Statistical Characteristics of Raindrop Size Distributions Observed in East China during the Asian Summer Monsoon Season using 2D-Video Disdrometer and Micro-rain Radar Data

Long Wen[1], Kun Zhao[1], Guifu Zhang[1,2], Ming Xue[1,2], Bowen Zhou[1]
Su Liu[1], and Xingchao Chen[1]

[1]Key Laboratory of Mesoscale Severe Weather/MOE and School of Atmospheric Sciences, Nanjing University, 163 Xianlin Road, Nanjing 210023, China

[2]Center for Analysis and Prediction of Storms and School of Meteorology, University of Oklahoma, Norman Oklahoma 73072, USA

Submitted to Journal of Geophysical Research-Atmospheres

Revised and accepted in February 2016

Corresponding author address:

Dr. Kun Zhao
Key Laboratory of Mesoscale Severe Weather/MOE,
School of Atmospheric Sciences, Nanjing University,
163 Xianlin Road, Nanjing 210023, China
Email: zhaokun@nju.edu.cn

Key points:
(1) First report of 2DVD and MRR measurements in East China during summer monsoon season.
(2) Structure and DSD of convective, stratiform and shallow precipitation types.
(3) Intra-summer variation of DSD and radar rainfall estimation relation.

Abstract

The characteristics of raindrop size distributions (DSDs) and vertical structures of rainfall during the Asian summer monsoon season in East China are studied using measurements from a ground-based two-dimensional video disdrometer (2DVD) and a vertically-pointing micro-rain radar (MRR). Based on rainfall intensity and vertical structure of radar reflectivity, the observed rainfall is classified into convective, stratiform and shallow precipitation types. Among them, shallow precipitation has previously been ignored or treated as outliers due to limitations in traditional surface measurements. Using advanced instruments of 2DVD and MRR, the characteristics of shallow precipitation are quantified. Furthermore, summer rainfall in the study region is found to consist mainly of stratiform rain in terms of frequency of occurrence, but is dominated by convective rain in terms of accumulated rainfall amount. Further separation of the summer season into time periods before, during and after the Meiyu season reveals that intra-summer variation of DSDs is mainly due to changes in percentage occurrence of the three precipitation types, while the characteristics of each type remain largely unchanged throughout the summer. Overall, higher raindrop concentrations and smaller diameters are found compared to monsoon precipitation at other locations in Asia. Higher local aerosol concentration is speculated to be the cause. Finally, rainfall estimation relationships using polarimetric radar measurements are derived and discussed. These new relationships agree well with rain gauge measurements and are more accurate than traditional relations, especially at high and low rain rates.

1. Introduction

Raindrop size distribution (DSD) is a fundamental microphysical property of precipitation. Understanding the variability of DSD is important for improving quantitative precipitation estimation (QPE) and microphysics parameterization in numerical weather prediction (NWP) models for accurate quantitative precipitation forecast (QPF) [*Milbrandt and Yau*, 2005; *Sun*, 2005; *Zhang et al.*, 2006]. For several decades, rain DSDs have been studied around the world using surface disdrometer measurements and are known to vary both spatially and temporally across different precipitation types, climatic regimes and orography [*Ulbrich*, 1983; *Tokay and Short*, 1996; *Testud et al.*, 2001; *Zhang et al.*, 2001; *Bringi et al.*, 2003; *Rosenfeld and Ulbrich*, 2003]. Various radar-based QPE algorithms have been developed using these DSD observations. These algorithms include *Z-R* relations and polarimetric radar algorithms, where *Z* and *R* are the radar reflectivity factor and rain rate [e.g., *Marshall and Palmer*, 1948; *Rosenfeld et al.*, 1993; *Bringi and Chandrasekar*, 2001; *Ryzhkov et al.*, 2005; *You et al.*, 2014].

The climate in China is deeply influenced by monsoons. During the Asian summer monsoon season (May-August), southerly winds dominate and warm and moist air is transported from the ocean to the continent of China, increasing convective instability in the region. As a result, heavy precipitation episodes occur frequently in South and East China during the monsoon season. A quasi-stationary subtropical front, called the Meiyu front, is a prominent feature in the region [*Tao and Chen*, 1987]. The Meiyu front establishes its mean position over South China with the onset of the East Asian summer monsoon in the South China Sea, then moves northward to the Yangtze-Huaihe River Basin to establish the commonly known Meiyu season in the region. The Yangtze-Huaihe River Basin Meiyu season typically lasts from mid-June to mid-July, producing persistent heavy rainfall [*Ding and Chan*, 2005; *Xu et al.*, 2009; *Yu and Li*, 2012].

The DSDs in the Meiyu season over China have only received limited investigation. Chen et al. [2013] examined the statistical characteristics of DSDs during the Meiyu season at Nanjing China, using three-year observations from a first-generation one-dimensional (1D) laser-optical Particle Size Velocity (PARSIVEL) disdrometer manufactured by OTT-Germany. Their results show that the concentration of raindrops is slightly lower, and the median raindrop diameter is higher than those observed in some other subtropical locations and even during Baiu (Meiyu is named Baiu in Japan) in Japan [*Bringi et al.*, 2006; *Chen et al.*, 2013]. Tang et al. [2014] further examined DSDs in different climatological regions in China, and found that both North and South China have lower raindrop concentrations than East China during the summer.

Results from the cited papers are not conclusive. They are mostly limited to using surface disdrometer observations and they were plenty of measurement uncertainties. For example, the PARSIVEL disdrometer used generally underestimates small raindrops and overestimates large drops [*Tokay et al.*, 2013]. As such, it can artificially increase the measured median diameter of raindrops. With only surface-based measurements, it is also difficult to investigate the relationship between DSDs and the corresponding vertical structures of precipitation, which is important for DSD characterization. Finally, those studies focus mainly on precipitation during the Meiyu season; whether DSD varies significantly across the pre-Meiyu, Meiyu and post-Meiyu periods remains unknown [*Xu et al.*, 2009].

To improve the understanding of the dynamics and microphysics of severe convective systems, field campaigns of the OPACC (Observation, Prediction and Analysis of Severe Convection of China) project were conducted in the Yangtze-Huaihe River Basin in East China in the summers of 2014 and 2015. For the first time, a two-dimensional video disdrometer (2DVD) [*Schönhuber et al.*, 2007], a vertically pointing micro rain radar (MRR), and a wind profiler radar (WPR) were collocated to observe the precipitation microphysics in the east China region (Fig. 1). A one-dimensional PARSIVEL disdrometer was also collocated for comparison purpose. The purpose of this study is to examine the precipitation characteristics during the summer monsoon season in East China using this unique dataset. Unlike previous studies that usually separated precipitation into the convective and stratiform types, three types of precipitation (convective, stratiform and shallow) are identified in this study, and their DSDs and vertical structures are quantitatively compared among the pre-Meiyu, Meiyu and post-Meiyu periods. Furthermore, polarimetric rainfall estimators are derived from DSD observations and discussed as well.

2. Data and methods

2.1 Instruments and dataset

The datasets used in this study were collected at a national weather station in Jiangning (JN), Nanjing from June to August during the 2014 and 2015 OPACC summer field campaigns. Nanjing is located in the Yangtze-Huaihe River Basin of East China, a region strongly influenced by the East Asia Summer Monsoon in the summer. A picture of the field site (31.93°N, 118.90°E) is shown in Fig.1. The MRR and WPR were located nearby on the roof of a building, about 7 m above the ground and 20 m away from the 2DVD. The rain gauge (RG), OTT PARSIVEL and 2DVD were positioned no more than 3 m apart. The 2DVD used was the current third generation version manufactured by Joanneum Research in Graz, Austria (details can be found at www.distrometer.at). It accounts for the drops in the inner part of the measurement inlet only to reduce splash effects. The horizontal imaging resolution of the unit used in this study is approximately 0.2 mm while the vertical resolution is 0.1 − 0.2 mm for

raindrops depending on particle terminal velocity [*Schönhuber et al.*, 2007]. The OTT PARSIVEL disdrometer used, as in Chen et al. [2013], was the first-generation version, which measures 32 bins of diameter from 0 to 25 mm and 32 bins of fall speeds from 0 to 22.4 m s^{-1} [*Löffler-Mang and Joss*, 2000]. A size correction proposed by Battaglia et al. [2010] has been applied for the OTT PARSIVEL observations to minimize the measurement error. The vertically pointing MRR is a compact 24 GHz K-band frequency-modulated, continuous-wave (FM-CW) Doppler radar [*Peters et al.*, 2002]. It observes 30 vertical levels in the atmosphere with range-gate resolution set to 200 m. It is also capable of determining DSDs from the Doppler spectra utilizing the relation between drop size and terminal fall velocity according to Atlas et al. [1973]. The main limitation of MRR of such retrieval is that it does not account for wind (horizontal or vertical) at any scale. The temporal resolution is 1 min for 2DVD, MRR, PARSIVEL and RG, and 6 min for WPR in this study. In-situ sounding data were collected as well.

By screening the time series of DSD data, as well as composite radar reflectivity mosaic and rain gauge data from China Meteorological Administration (CMA), 27 precipitation episodes were identified (Fig. 2 and Table 1) for the two summer seasons, including four in the pre-Meiyu period, nine in the Meiyu period and fourteen in the post-Meiyu period. Following Carbone et al. [2002], a precipitation episode is defined as clusters of rain systems (mainly in the form of organized convection such as squall lines, mesoscale convective systems and frontal rainband) which exhibit coherent rainfall patterns, characteristic of propagating events, under a broad range of atmospheric conditions. The episodes are most easily identified in a time-longitude Hovmöller diagram [*Carbone et al.*, 2002]. In this study, the domain of computation for the Hovmöller diagrams is 2° × 2° centered at JN site. The Meiyu period in the Yangtze-Huaihe River Basin was between 23 June and 19 July in 2014 and between 24 June and 13 July in 2015, as officially determined by CMA. The pre-Meiyu period is from 1 Jun to a day before the onset of the Meiyu period, and the post-Meiyu period is from the end date of the Meiyu period to 31 August of each year. Figure 2 indicates that the 850 hPa winds during the precipitation periods are predominantly (over 90% of the time) southeasterly to southwesterly, with those during the Meiyu season being mostly southwesterly. A similar quality control method as used in Tokay et al. [2013] is used to process the 2DVD observations. For each 1-min data from the 2DVD, if the total number of drops is less than 10 or a disdrometer-derived rain rate is less than 0.1 mm h^{-1}, it is disregarded; otherwise it is considered to be a rainy minute. For each 1-min data from the MRR, if the rain rate observed by 2DVD is less than 0.1 mm h^{-1}, it is then discarded as noise caused by non-precipitation echo.

2.2 Raindrop size distribution

When the raindrop size distribution is given, the integral rainfall parameters including the radar reflectivity factor Z (mm^6 mm^{-3}), rain rate R (mm h^{-1}), liquid water content LWC (g m^{-3}) and the total concentration of raindrops N_t (m^{-3}) are derived

$$Z = \sum_{i=1}^{L} D_i^6 N(D_i) \Delta D_i, \tag{1}$$

$$R = \frac{6\pi}{10^4} \sum_{i=1}^{L} D_i^3 V_i N(D_i) \Delta D_i, \tag{2}$$

$$LWC = \frac{\pi}{6000} \sum_{i=1}^{L} D_i^3 N(D_i) \Delta D_i, \tag{3}$$

$$N_t = \sum_{i=1}^{L} N(D_i)\Delta D_i, \tag{4}$$

where L is the total number of bins, D_i (mm) is the equivalent spherical raindrop diameter for size-bin i, ΔD_i is the corresponding diameter interval (mm) and V_i (m s^{-1}) is the fall speed for the velocity-bin i. The equivalent-volume diameters are sorted into size categories of 0.2 mm. The range in tabulated raindrop diameters is 0.1 − 8.1 mm (41 bins), and the velocity bin is changed to match the size bin. V_i is obtained by averaging measured particle velocities within that size bin. $N(D_i)$ (mm^{-1} m^{-3}) represents the number concentration of drops with diameters in the range from $D_i - 0.5\Delta D_i$ to $D_i + 0.5\Delta D_i$ (per unit size interval).

The widely used three-parameter gamma-model DSD [*Ulbrich*, 1983] represents the observed raindrop spectra reasonably well [*Tokay and Short*, 1996]. The gamma size distribution is expressed as

$$N(D) = N_0 D^{\mu} \exp(-\Lambda D), \tag{5}$$

where D (mm) is the equivalent diameter and $N(D)$ (m^{-3} mm^{-1}) is the number concentration of raindrops in a unit volume of air and in the unit size interval. N_0 ($mm^{-1-\mu}$ m^{-3}), Λ (mm^{-1}) and μ (dimensionless) are the concentration, the slope and the shape parameters, respectively. The *n*th-order moment of the DSDs is expressed as

$$M_n = \int_0^{D_{\max}} D^n N(D) dD. \tag{6}$$

The mass-weighted mean diameter D_m (mm) equals the ratio of the 4th to the 3rd moment of the size distribution

$$D_m = \frac{M_4}{M_3}, \tag{7}$$

and the generalized intercept parameter N_w (mm^{-1} m^{-3}) was computed as [*Bringi et al.*, 2003]

$$N_w = \frac{4^4}{\pi \rho_w}\left(\frac{10^3 W}{D_m^4}\right), \tag{8}$$

where ρ_w (assumed to be 1.0 g cm^{-3}) is the density of water.

The standard deviation of the mass spectrum (σ_m) with respect to D_m is defined as [*Ulbrich*, 1983]

$$\sigma_m^2 = \frac{\int_0^{D_{\max}} (D - D_m)^2 D^3 N(D) dD}{\int_0^{D_{\max}} D^3 N(D) dD}. \tag{9}$$

Note that D_m, N_w and σ_m are also calculated directly from measured DSD and not by fitting the measurements to the gamma model.

2.3 Polarimetric radar parameters

Polarimetric radar parameters, such as radar reflectivity in horizontal polarization Z_H ($10\log_{10}(Z_h)$) and differential reflectivity Z_{DR}, provide valuable information that can better characterize DSD variability and estimate precipitation. They are most important for improving the accuracy of rainfall estimation. These variables depend on the DSD and the drop scattering amplitudes as follows:

$$Z_{h,v} = \frac{4\lambda^4}{\pi^4 |K_w|^2} \int_{D_{\min}}^{D_{\max}} \left| f_{hh,vv}(D) \right|^2 N(D) dD, \tag{10}$$

$$Z_{DR} = 10\log_{10}(\frac{Z_h}{Z_v}), \tag{11}$$

where λ is the radar wavelength, K_w is the dielectric factor of water and $f_{hh,vv}(D)$ are the backscattering amplitudes of a drop at horizontal or vertical polarization.

The polarimetric radar parameters in Eq. 10-11 were calculated from the observed DSDs by 2DVD using the T-matrix [*Ishimaru*, 1991] scattering techniques described by Zhang et al. [2001]. Since the effects of temperature on radar observables at S-band are negligibly small [*Aydin and Giridhar*, 1992], the raindrop temperature was assumed to be 10°C in this study. The raindrops were also assumed to follow the Brandes axis ratio relation [*Brandes et al.*, 2002].

2.4 Classification of rain types

Previous studies have usually categorized precipitation into stratiform and convective types based on the rainfall intensity and variation measured by surface disdrometers [*Tokay and Short*, 1996; *Testud et al.*, 2001; *Bringi et al.*, 2003; *Chen et al.*, 2013]. A few researchers suggested a third type of precipitation (named shallow precipitation) based on data from the vertically-pointing radar observations, which are characterized by low cloud top (below 0 °C isotherm) and weak rainfall rate [*Fabry and Zawadzki*, 1995; *Cha et al.*, 2009]. However, shallow rainfall has generally been ignored or recognized as stratiform rain by surface disdrometer-based classification schemes.

In this study, three types of precipitation, including stratiform, convective and shallow, are defined by combining the rainfall intensity and the vertical structure of radar reflectivity measured by the 2DVD and the MRR. Figure 3 presents an example of the measured vertical profile of reflectivity and the time series of the DSDs using the MRR and the 2DVD from 0000 to 2400 UTC 12 July 2014. The convective, stratiform and shallow categories are indicated by red, black and purple bars, respectively, on the top of Fig. 3a. The feature of the shallow rain, as shown in Fig. 3, has a notable difference compared to the convective and stratiform rain. While the bright band is a marked feature of stratiform precipitation, the top of radar echo of shallow rain is too low to reach the melting layer, which means that the precipitation forms directly in liquid form and no melting is present [*Fabry and Zawadzki*, 1995; *Cha et al.*, 2009]. The corresponding DSDs of this shallow rain have a relatively small maximum diameter and high concentration of raindrops with small diameters, indicating distinctions among the microphysical processes of the three precipitation types.

The rain type classification scheme is a two-step procedure. First, a method similar to that used in Bringi et al. [2003] and Chen et al. [2013] is used to classify precipitation into stratiform and convective parts. The time rate change of R and the standard deviation, σ_R, observed by 2DVD is used to separate convective from stratiform rain types. Specifically, over at least 10 consecutive 1-min DSD samples, if the R values are higher than 0.5 mm h^{-1} and the standard deviation σ_R is less than 1.5 mm h^{-1}, then the precipitation is classified as stratiform; otherwise if the R values are higher than 5 mm h^{-1} and the standard deviation σ_R is more than 1.5 mm h^{-1}, then it is classified as convective rain. Samples that belong neither to the stratiform nor convective type are excluded from the investigation. Next, similar to Cha et al. [2009] and Fabry and Zawadzki [1995], the time series of vertical reflectivity measured by MRR is used to separate shallow rain from within the stratiform type identified in step 1. Specifically, for the time series of vertical profiles of reflectivity measured by the MRR during the stratiform processes, if the echo top of radar reflectivity is 1 km lower than the level of

the 0° C isotherm, then it is recognized as shallow rain. The rest of the precipitation are recognized as stratiform rain.

The classification scheme produces 2,701 convective samples, 6,882 stratiform samples and 1,530 shallow samples, as presented in Table 2. The fraction of uncategorized rainfall is about 11.3% in terms of total rainfall contribution and 21.1% in terms of occurrence frequency. The mean rain rates for convective, stratiform and shallow rains are approximately 24.44, 2.35 and 1.95 mm h^{-1}. The frequency of occurrence and the corresponding contribution to the total categorized rainfall are, respectively, 24.3 % and 77.5 % for convective rain, 61.9 % and 19.0 % for stratiform rain, and 13.8 % and 3.5 % for shallow rain. Note that, although the percentage of shallow rain precipitation is small, it may have important roles in, e.g., atmospheric energy balance (for example, affecting the vertical distribution of latent heating [*Johnson et al.*, 1999] by moistening the lower troposphere [*Masunaga and Kummerow*, 2006]). Therefore, understanding the microphysics of shallow rain is also important. The characteristics of shallow rain over tropical oceans and its role in maritime precipitation have been examined in quite a few studies [i.e. *Liu et al.*, 1995; *Short and Nakamura*, 2000; *Blyth et al.*, 2013; *Hamada et al.*, 2015; *Thompson et al.*, 2015]. But over continents, shallow rain has received little attention. We therefore include this category in our study.

3. Results and discussion

3.1 Vertical structure of precipitation

For different types of rain, the microphysical processes during the formation and landing of raindrops are typically different. Therefore, investigating the vertical profiles of radar reflectivity (VPR, reflectivity greater than 15 dBZ) helps to improve the understanding of the microphysical processes of precipitation. Figure 4 presents the VPR in terms of contoured frequency-by-altitude diagrams [CFAD, *Yuter and Houze Jr*, 1995] for the three different rain types measured by MRR. The level of the 0° C isotherm (gray line; about 5,226 m from the ground level) is averaged by all the in-situ sounding data, which are three times a day during the precipitation episodes.

The convective CFAD in Fig. 4a has a near absence of low reflectivity (＜25 dBZ) near the ground. The reflectivity ranges from 25 dBZ to 53 dBZ with an average value of 38 dBZ. The reflectivity decreases dramatically with height, which can be attributed to the strong reflectivity-attenuation in heavy rainfall, as mentioned by Tsai and Yu [2012] and Wen et al. [2015]. Therefore, only the data from the lowest heights (~200m) are quantified for convective rain here, in order to avoid the effect of attenuation on the physical explanation of VPR.

In contrast to convective rain, the stratiform CFAD in Fig. 4b indicates a frequent occurrence of weak reflectivity below 4.5 km, with a mean value of about 25 dBZ that stays nearly constant with decreasing height, suggesting that the raindrop evaporation and coalescence are in near balance in stratiform rain. The enhanced radar echo area (known as the bright band) has been detected around 4.6 km, which is 0.6 km below the averaged sounding 0° C isotherm (~ 5,226 m). The top of the bright band can be considered the melting level and the altitude of the 0° C isotherm [*Glickman*, 2000], which means that the position of 0° C isotherm indicated by the MRR and sounding agree well with each other. Above that level, the stratiform reflectivity decreases sharply with height to a minimum centered at about 16 dBZ, and an extremely tight frequency distribution within ±5 dBZ, representing a nearly homogenous field of reflectivity at each level.

Compared to the convective and stratiform rain, the reflectivity of shallow rain is

the weakest. The shallow CFAD in Fig. 4c implies a distinctive, narrower frequency distribution. The "modal distribution" ($>50\%$ of the maximum frequency in the distribution, see Hence and Houze [2011]) falls in the range of 15 to approximately 22 dBZ, with an average value centered at about 18 dBZ. The modal distribution of shallow rain reaches 1.5 km, while the "outlier distribution" ($<50\%$ of the maximum frequency) reaches approximately 3.5 km and extends to about 28 dBZ. The VPR stays nearly constant with height but far below the melting layer, which means that the precipitation forms directly in liquid form and no ice phase is present. In other words, the warm precipitation process is dominant in shallow rain. The corresponding DSDs of this shallow rain have a relatively small maximum diameter and high concentration of raindrops with small diameters near the ground (as will be shown in Fig. 5d).

3.2 Distributions of D_m and N_w

Figure 5 shows the relative frequency histograms of D_m and $\log_{10} N_w$ for the total categorized dataset and for the convective, stratiform and shallow subsets calculated from the 2DVD, as well as three key parameters: mean, standard deviation and skewness. For the total categorized dataset (Fig. 5a), D_m and $\log_{10} N_w$ histograms are both positively skewed. The standard deviations of the histograms are large (0.34 mm for D_m and 0.61 for $\log_{10} N_w$), which suggest a high variability in D_m and N_w. Note that the units of N_w are in $m^{-3}\,mm^{-1}$ and the Marshall-Palmer value of $\log_{10} N_w$ for exponential shape is 3.9 ($\log_{10}$ (mm^{-1} m^{-3}), omitted hereafter). When considering different rain types, it is found that the D_m histograms are all positively skewed, whereas the $\log_{10} N_w$ histograms exhibit negative skewness for shallow rain (see Figs. 5b-d). Shallow rain histograms show higher skewness for both D_m and $\log_{10} N_w$ when compared with convective and stratiform rain. The convective rain histograms of D_m and $\log_{10} N_w$ tend to shift toward the large values relative to stratiform rain histogram, indicating that convective rain has higher D_m and N_w values. Shallow rain has the smallest D_m (highest $\log_{10} N_w$), the mean value of which is about 0.64 mm (4.97), compared with 1.41 mm (4.37) and 1.16 mm (3.78) for convective and stratiform rain, respectively.

Figure 6 shows the scatter plot of $\log_{10} N_w$ versus D_m for the three rain types, as well as statistical results from similar climatic regimes (i.e. East China, Japan and Taiwan, where the climates are deeply influenced by EASM) reported by Bringi et al. [2006], Chen and Lin [2009] and Chen et al. [2013]. The two gray rectangles correspond to the maritime and continental convective clusters reported by Bringi et al. [2003]. The convective rain of our study is mostly plotted over the "maritime-cluster," and only a few points appear in the "continental-cluster" even though Nanjing is located in the inland area. This result indicates that the summer convective rain in East China is more of a maritime nature. The stratiform rain is plotted over a wide range, from 0.5 to 3.0 mm for D_m and 2.0 to 5.7 for $\log_{10} N_w$, respectively. Nearly 72% of the stratiform rain appear on the left side of the "stratiform line" (magenta dashed line in Fig. 6) given by Bringi et al. [2003]. The N_w-D_m pair for the total categorized dataset (red cross) is very close to the stratiform line reported by Bringi et al. ([2003]; magenta dashed line), due to the highest population of stratiform in the summer monsoon season (as shown in Table 2). Note that the unusual stratiform points with $D_m \approx 2.0-3.0$ mm and $\log_{10} N_w \approx 2.0-2.75$ are caused by a squall line, and the understanding of the exact microphysical processes responsible for these points is beyond the scope of this paper. The majority of shallow points is within the area of $D_m \approx 0.5-1.0$ mm and $\log_{10} N_w \approx 4.0-5.8$.

The DSDs measured in this study indicate a lower value of D_m and a higher value of $\log_{10} N_w$ (the mean values are 1.15 mm and 4.09) compared with the 2DVD measurements of Baiu (Meiyu in Japan) in Okinawa, Japan ([*Bringi et al.*, 2006]; where the mean values are 1.47 mm and 3.78), and Meiyu in Taiwan during the Southwest Monsoon Experiment (SoWMEX) ([*Chen and Lin*, 2009]; where the mean values were 1.40 mm and 3.55). Given that all three studies use the same type of instrument (i.e. 2DVD) to measure the DSDs of precipitation systems within the East Asian Summer Monsoon, assuming minimum inter-annual variations, the differences in the DSD characteristics are likely to be related to the specific geographical locations.

One possible reason for such differences could be the aerosol concentration differences across the regions. In East China, especially in the Yangtze River Delta region, the concentration of aerosols is markedly higher [*Streets et al.*, 2008; *Liu et al.*, 2011]. During the Asian summer monsoon season (May-August), abundant moisture is transported from the ocean inland. In the presence of high aerosol concentration therefore plenty of condensation nuclei's, an adequate supply of moisture tends to lead to higher concentrations of smaller raindrops. In contrast, the aerosol concentration is relatively low over the islands of Japan and Taiwan, and fewer but larger raindrops tend to form mainly through collision-coalescence process. It is noted the DSDs from our 2DVD measurements are also different from those obtained from the Meiyu season in Nanjing, China using a 1D PARSIVEL disdrometer ([*Chen et al.*, 2013]. The use of different instruments may be the main cause, as will be discussed more later.

To investigate the variability of the two parameters with respect to rain types and rain rates, scatter plots of $D_m - R$ and fitted power-law relationships with different rain types are shown in Fig. 7. For both $D_m - R$ and $N_w - R$ (not shown), the exponents in the relationships are positive, suggesting that the D_m and N_w values are enhanced with rain intensity, possibly due to more efficient coalescence and breakup mechanisms [*Chen et al.*, 2013]. It is notable that at high rain rates, the DSDs may reach an equilibrium state where coalescence and breakup of raindrops are in near balance [*Hu and Srivastava*, 1995]. Under the equilibrium condition, D_m stays at a constant value, and any increase in rain rate is mainly due to an increase in N_w [*Bringi and Chandrasekar*, 2001]. As can be seen from Fig. 7a, the D_m values approach a stable value around 1.6 – 1.8 mm for $R > 100$ mm h^{-1}, indicating that the DSDs may have reached an equilibrium state. The stratiform rain has the largest coefficient and exponent values of $D_m - R$ relation (Fig. 7c) among the three rain types. Hence, for a given rain rate, stratiform rain has the highest D_m values compared with the convective and shallow rain. For example, when R is 20 mm h^{-1}, the D_m values are 1.44 mm, 1.65 mm and 0.91 mm for convective, stratiform and shallow rain, respectively. The coefficient and exponent values of the $D_m - R$ relation are slightly lower for the convective rain (Fig. 7b) and the lowest for the shallow rain (Fig. 7d). Moreover, the observed maximum rain rate of shallow rain is only 8.2 mm h^{-1} while the values of D_m are mostly under 1 mm. As a result, the corresponding contribution to the total rainfall (3.5%) is negligible, even though the raindrop concentration of shallow rain is extremely high.

3.3 Composite raindrop spectra

The characteristics of the DSD shapes of the total categorized dataset and of the three rain types are presented in Fig. 8. The composite drop size spectra are obtained by averaging the instant size spectra for each rain type. The integral rain parameters derived from the composite spectra are listed in Table 3. Note that the maximum possible raindrop diameter is defined as the diameter of the last bin in the composite

spectra whose number concentration is greater than 1.0×10^{-3} m^{-3} mm^{-1}, as is done in Chen et al. [2013].

The composite spectra exhibit similar one-peak distributions in all three rain types (Fig. 8). Nevertheless, there are distinct differences in the DSDs. The maximum raindrop diameter for convective, stratiform and shallow rain is 6.3, 4.5 and 2.9 mm, respectively. When compared to the other two rain types, the convective spectrum has the highest concentrations at all size ranges, resulting in a higher number concentration, a higher rain rate and more rain water content (see Table 3). The peak concentration appears near the low limit of drop size that the disdrometer can measure. The stratiform spectrum is narrower and that of shallow convection is the narrowest. The latter also has much higher concentrations below 1.1 mm, resulting in higher rain water contents (see also Table 3). Due to the unreliability of measurements of small drops under 0.5 mm, we will not discuss that part of the spectrum.

When compared with the composite raindrop spectrum of Chen et al. [2013], the most obvious difference is that the spectra of our study have higher concentrations of raindrops, especially in small drop size in both stratiform and convective rain type. For reference, the composite spectrum of two years of Meiyu precipitation data obtained from 2DVD and in situ PARSIVEL (the same instrument as that used in Chen et al. [2013]) are also shown at the upper right corner of Fig. 8. As can be seen, the PARSIVEL disdrometer generally underestimates small raindrops and overestimates large drops when compared to that of 2DVD. Tokay et al. [2013] noticed the same in their study. Accordingly, the higher value of $\log_{10} N_w$ and lower value of D_m obtained from 2DVD than those from PARSIVEL mentioned in section 3.2 can at least be partly attributed to the instrument differences.

3.4 Comparison of different periods

To investigate the DSD differences during different precipitation periods, we define the pre-Meiyu, Meiyu and post-Meiyu periods (see Section 2.1). The integral rain parameters of the three periods are derived from the composite spectra and listed in Table 4. Figure 9 shows the percentage occurrence of different rain types during each precipitation period. The occurrence of convective rain stays around $25 - 30$ % throughout. Due to the significant increase of shallow rain, the stratiform rain decreases abruptly from nearly 70 % in the pre-Meiyu and Meiyu periods to 55 % in the post-Meiyu period. For the total categorized rainfall (Table 2), the contribution to precipitation amount in the summer monsoon seasons of 2014 and 2015 in the study area is dominated by convective rain (77.5 %) while stratiform rain occurs most frequently (61.9 %). These results are consistent with those of previous studies using three years of ground-based disdrometer data [*Chen et al.*, 2013] or ten years of TRMM PR measurements [*Liu et al.*, 2012].

The average values of D_m and $\log_{10} N_w$ for the three rain types during the different precipitation periods are given in Fig. 9 as well. For each rain types, the average D_m and $\log_{10} N_w$ values in pre-Meiyu and Meiyu period show slight difference except that the $\log_{10} N_w$ for shallow rain decrease moderately from 5.14 to 5.00. In post-Meiyu, the average $\log_{10} N_w$ values show moderate increase for convective and stratiform rain and the average D_m values decrease a little for convective rain. Overall, there are no distinct differences in the average D_m and $\log_{10} N_w$ values for each rain type across the different precipitation periods. This suggests that the characteristics of each rain type remain unchanged during the whole monsoon period.

The occurrence frequency of various parameters (the mass-weighted diameter D_m, the generalized intercept parameter N_w, the liquid water content *LWC* and the standard

deviation of the mass spectrum σ_m) are computed to investigate the variability of the four parameters across the pre-Meiyu, Meiyu and post-Meiyu periods. The occurrence frequency is defined as the number of occurrences for a specific value normalized by the total number of samples. As shown in Fig. 10a, D_m decreases from the pre-Meiyu period to the post-Meiyu period. The peak value of the D_m distribution curve appears at 1.3 mm for the pre-Meiyu period and at 1.1 mm for the Meiyu period, which is approximately equal to the mean D_m value of the stratiform rain for each period, 1.24 mm and 1.18 mm, as given in Fig. 9. Because of the significant increase in shallow rain, double-peak distribution results for the post-Meiyu period, where the values appear at 0.7 mm and 1.3 mm. i.e. one peak (1.3 mm) approximately equal to the mean D_m value of the stratiform rain while the other peak (0.7 mm) is attributed to the significant increase in shallow rain during the post-Meiyu period. Similarly, the distribution $\log_{10} N_w$ shows a two-peak pattern for the post-Meiyu period as well, and $\log_{10} N_w$ around the second peak is larger than the other two periods (also see Table 4). However, there are only slight differences in liquid water content (*LWC*) among the three periods (Fig. 10c and Table 4). The Meiyu period shows the lowest *LWC* values compared to the other periods, as the mean values of *LWC* are 0.57, 0.44 and 0.50 g m^{-3} for the pre-Meiyu, Meiyu and post-Meiyu periods, respectively. Such variations of *LWC* can be explained by Eq. (3), where *LWC* depends on both raindrop diameter ($\sim D^3$) and number concentration *N(D)*. The convective rain has the largest raindrop size, hence the highest *LWC* among all three types of precipitation. Compared with stratiform rain, shallow rain has a lower *D* but a higher *N(D)*, so they contain almost the same *LWC*. As the Meiyu period has the lowest occurrence frequency of convective rain, it therefore has the lowest *LWC* among three periods. The distribution of σ_m has little difference between the pre-Meiyu and Meiyu periods while the post-Meiyu period shows the narrowest spectrum with the integral distribution becoming narrower and yielding smaller values, due to the abundance of shallow rain.

The above analyses indicate that the DSDs of each rain type during the three precipitation periods from summers of 2014 and 2015 differ only slightly. The difference in the occurrence frequency of various DSD parameters for different precipitation periods seems to have been due more to the difference in the dominant precipitation type in each period than to the change in season. Specifically, the pre-Meiyu period contained a higher percentage of convective rain episodes that were associated with well-organized mesoscale convective systems while the Meiyu rainfall had the largest fraction of stratiform rain, and the post-Meiyu period, in contrast, had a significant increase in shallow rain.

3.5 Rainfall estimation relationships

Based on the characteristics of DSDs in the summer monsoon season over East China, radar-based rainfall estimation algorithms are discussed in this section. The most widely used radar QPE algorithm is the *Z-R* relation. However, the diversity of DSDs due to rain types, geographical locations, climatic regimes, and even the choice of disdrometers, will result in different coefficients in the *Z-R* relation [*Chandrasekar et al.*, 2003; *Rosenfeld and Ulbrich*, 2003; *Tokay et al.*, 2008]. For example, the National Weather Service's (NWS) Weather Surveillance Radar-1988 Doppler precipitation processing subsystem recommends $Z = 250R^{1.2}$ [*Rosenfeld et al.*, 1993] for tropical systems, and Chen et al.[2013] suggests $Z = 368R^{1.21}$ for Meiyu systems. Thus, a better understanding of the characteristics of the DSD in East China during the summer monsoon season is needed to help us improve radar rainfall estimation in this region.

Scatter plots between *Z* and *R* for the total categorized dataset and for the three

rain types are presented in Fig. 11. The coefficient and exponent values of the fitted power-law equations are provided with the corresponding colors. In order to facilitate the comparison of *Z-R* relation with different rain types, $Z = 368R^{1.21}$ [*Chen et al.*, 2013] for convective rain in Meiyu season and $Z = 200R^{1.6}$ [*Marshall and Palmer*, 1948] for continental stratiform rain are also provided. The former $Z = 368R^{1.21}$ relationship is slightly to the right of our $Z = 230.85R^{1.34}$ relationship for convective rain at high rain rates. In other words, it gives a higher R value for a given Z, which indicates that $Z = 368R^{1.21}$ would overestimate rainfall, in particular at high rain rates. For example, when Z is 1.0×10^5 mm^6 m^{-3} (50 dBZ, which happens frequently in summer rainfall), the rain rate is overestimated by about 25% with the former $Z = 368R^{1.21}$ relationship. As shown in Fig. 11, our new $Z = 232.44R^{1.34}$ relationship for the total categorized dataset fits the measured data well, in particular with the new relationship for convective rain, although it underestimates the rainfall at low rain rates. This again suggests that the contribution of precipitation in summer monsoon season is mainly dominated by convective rain.

The new relationships for the three rain types are typically different from each other. Although the raindrop concentration is the highest for shallow rain, the new $Z = 41.68R^{1.68}$ relationship for shallow rain lies to the lower-right of the other two relationships. This is because radar reflectivity is more sensitive to raindrop diameter D than to raindrop concentration $N(D)$, as can be concluded from Eq. (1) or the combination of Figs. 4 and 5. Thus, for a given Z, the shallow *Z-R* relationship would estimate a higher R value than the stratiform *Z-R* relationship. The distinct difference between the shallow and stratiform *Z-R* relationships suggests that there are two different types of precipitation. Furthermore, overestimating rainfall by previous stratiform *Z-R* relationships might be partly due to the erroneous classification of shallow rain as stratiform rain by surface disdrometer-based schemes.

The above analysis, as well as previous studies, suggests that DSD variability is a major source of diversity of *Z-R* relations. Since the accuracy of remote estimation of rainfall is limited by and progress is impeded by the variety of DSDs and sampling errors, researchers have turned to fixed-form relations of polarimetric measurements which provide additional parameters. Recent studies indicate that rainfall estimates made with the radar reflectivity (Z_H) and differential reflectivity (Z_{DR}) measurement pair are sensitive to size variations. They help to improve rainfall estimates derived only from radar reflectivity [*Zhang et al.*, 2001; *Brandes et al.*, 2002; *Ryzhkov et al.*, 2005; *Lee*, 2006; *Cao et al.*, 2008; *Cao et al.*, 2010; *You et al.*, 2014]. In this study, S-band polarimetric radar parameters Z_H and Z_{DR} are calculated following Zhang et al. [2001] for Brandes drop shape assumption using 2DVD data observed during the summer. A power-law rainfall estimation relationship is then determined by the least squares method and the $R(Z_H, Z_{DR})$ is given by

$$R = 1.81 \times 10^{-3} Z_H^{0.968} Z_{DR}^{-0.86}, \tag{12}$$

where Z_H ranges from $10^{1.5}$ to $10^{5.6}$ mm^6 m^{-3} and Z_{DR} ranges from 0.1 to 3 dB, similar to Aydin and Giridhar [1992].

Figure 12 shows the scatter plots of 2DVD observed hourly rainfall against the rainfall from the rainfall estimation relationship $R(Z_H, Z_{DR})$. To ensure a rigorous assessment, no threshold is set for either observed or estimated rainfall. The results of the statistical evaluation are given as well. The correlation coefficient (CC), standard deviation (STD) and root mean square error (RMSE) between $R(Z_H, Z_{DR})$-estimated and observed rainfall are 0.997, 0.524 and 0.534, respectively. The results suggest that the polarimetric estimates agree well with observations on the whole. These estimates

perform well even when low rain rates (where Z_{DR} measurement errors could be important) are included.

The disadvantage of the *Z-R* relation is that it is not unique and depends on DSDs, which vary both spatially and temporally across differing precipitation types, climatic regimes and orography. The $R(Z_H, Z_{DR})$ estimator has the advantage over the single-parameter estimator (*Z-R* relation) because it partially accounts for changes in median drop size through the Z_{DR} parameter. This capability reduces the impact of DSD variability on the quality of rainfall estimation [*Brandes et al.*, 2002; *Ryzhkov et al.*, 2005]. That is to say, without classification of rain types, rainfall estimation is consequently more accurate with additional polarimetric observations.

4. Summary and conclusions

In this paper, the characteristics of the raindrop size distributions (DSDs) and calculated polarimetric radar parameters of precipitation episodes during the Asian summer monsoon season are studied. For the first time, measurements from ground-based 2D video disdrometer and vertically pointing Micro-rain radar are utilized to improve characterization of summer precipitation in East China. A total of 27 precipitation episodes and 11,113 1-min DSD spectra are obtained for the summers of 2014 and 2015 at a site located in Nanjing in the Yangtze-Huaihe River Basin of East China. Combining the rainfall intensity and the vertical structure of radar reflectivity, convective, stratiform and shallow rain types are identified, and their DSDs and vertical structures are further compared among different precipitation periods (pre-Meiyu, Meiyu and post-Meiyu). Single-polarization and polarimetric rainfall estimators are derived from DSD observations and discussed as well. The main conclusions can be summarized as follows:

(1) The use of 2DVD and MRR observations enabled the identification of shallow rain in this study, which had generally been ignored or mistakenly recognized as stratiform rain in previous studies. Compared to the convective and stratiform rain, the reflectivity of shallow rain is the weakest. The vertical profiles of reflectivity shows that the shallow precipitation forms mostly through warm rain processes. The shallow rain DSDs have a relatively small maximum diameter and high concentrations with small diameters near the ground.

(2) The rainfall in the two summers studied at the measurement site is found to consist mainly of stratiform rain in terms of frequency of occurrence, but is dominated by convective rain in terms of accumulated rainfall amount. Relatively low values of D_m but high values of N_w are observed for all three rain types when compared with observations from similar climatic regimes (i.e. East China, Japan and Taiwan). This is likely associated with high local atmospheric aerosol and moisture contents. In the presence of high aerosol concentration, adequate supply of moisture leads to a higher raindrop concentration but lower raindrop diameter.

(3) The differences of the frequency distributions of various parameters during different precipitation periods appear to be due more to percentage occurrence variations among the three rain types, than to variation within each rain type. In other words, the characteristics of each precipitation type remain largely unchanged during the summer, although they occur at different frequencies before and after Meiyu.

(4) Radar-based rainfall estimation algorithms, $R(Z_H)$ and $R(Z_H, Z_{DR})$, are also derived and discussed. The *Z-R* relationships obtained are $Z = 230.85R^{1.34}$, $Z = 193.73R^{1.54}$, and $Z = 41.68R^{1.68}$ for convective, stratiform and shallow rain, respectively. In comparison, the single polarimetric $R(Z_H, Z_{DR})$ algorithm agrees well with rainfall observations for all rain types. The $R(Z_H, Z_{DR})$ estimator has the advantage over the

single-parameter estimator (*Z-R* relation) because it accounts for DSD differences through the additional Z_{DR} parameter.

Although interesting findings were obtained on the DSD characteristics of different types of summer precipitation in East China using two years of data from two types of disdrometer and an MRR, the results are not necessarily conclusive due to the still limited sample size of precipitation events. Long-term observations should be used as more data are collected. The vertical profiles of drop size spectra from MRR can be used to better understand the growth of raindrops in the shallow rain. The aerosol effects on DSDs are not yet well understood [*Rosenfeld et al.*, 2008; *May et al.*, 2011; *Tao et al.*, 2012], and aerosol observations are needed to determine the relation between the raindrop size and high-CCN. Moreover, high-resolution simulations with microphysics schemes properly accounting the effects of aerosol will be helpful for understanding the microphysical processes involved. We plan to conduct some of the research in the future.

Acknowledgements: This work was primarily supported by the National Fundamental Research 973 Program of China (2013CB430101) the National Natural Science Foundation of China (grants 41275031 , 41322032 and 41475015) and Social Common Wealth Research Program (GYHY201006007). Observational data used in this study were collected by a National 973 Project (2013CB430101). Due to its data policy, the DSD and MRR data cannot be released publically until 2018. Special requests for the data can be made at http://scw973.nju.edu.cn/ or contacting the project office at yang.zhengwei@nju.edu.cn. After 2018, the data of this paper will be uploaded to http://www.nersc.gov/users/science-gate-ways/ for public sharing. We also thank the Editor and three anonymous reviewers for their valuable suggestions that improved our paper.

References

Atlas, D., R. Srivastava, and R. S. Sekhon (1973), Doppler radar characteristics of precipitation at vertical incidence, *Reviews of Geophysics*, *11*(1), 1-35.

Aydin, K., and V. Giridhar (1992), C-band dual-polarization radar observables in rain, *Journal of Atmospheric and Oceanic Technology*, *9*(4), 383-390.

Battaglia, A., E. Rustemeier, A. Tokay, U. Blahak, and C. Simmer (2010), PARSIVEL snow observations: A critical assessment, *Journal of Atmospheric and Oceanic Technology*, *27*(2), 333-344.

Blyth, A. M., J. H. Lowenstein, Y. Huang, Z. Cui, S. Davies, and K. S. Carslaw (2013), The production of warm rain in shallow maritime cumulus clouds, *Quarterly Journal of the Royal Meteorological Society*, *139*(670), 20-31.

Brandes, E. A., G. Zhang, and J. Vivekanandan (2002), Experiments in rainfall estimation with a polarimetric radar in a subtropical environment, *Journal of Applied Meteorology*, *41*(6), 674-685.

Bringi, V., and V. Chandrasekar (2001), *Polarimetric Doppler weather radar: principles and applications*, Cambridge University Press.

Bringi, V., V. Chandrasekar, J. Hubbert, E. Gorgucci, W. L. Randeu, and M. Schoenhuber (2003), Raindrop Size Distribution in Different Climatic Regimes from Disdrometer and Dual-Polarized Radar Analysis, *Journal of the Atmospheric Sciences*, *60*(2), 354-365.

Bringi, V., M. Thurai, K. Nakagawa, G. HUANG, T. KOBAYASHI, A. ADACHI, H. HANADO, and S. SEKIZAWA (2006), Rainfall Estimation from C-Band Polarimetric Radar in Okinawa, Japan: Comparisons with 2D-Video Disdrometer and 400MHz Wind Profiler, *Journal of the Meteorological Society of Japan. Ser. II*, *84*(4), 705-724.

Cao, Q., G. Zhang, E. A. Brandes, and T. J. Schuur (2010), Polarimetric radar rain estimation through retrieval of drop size distribution using a Bayesian approach, *Journal of Applied Meteorology and Climatology*, *49*(5), 973-990.

Cao, Q., G. Zhang, E. Brandes, T. Schuur, A. Ryzhkov, and K. Ikeda (2008), Analysis of video disdrometer and polarimetric radar data to characterize rain microphysics in Oklahoma, *Journal of Applied Meteorology and Climatology*, *47*(8), 2238-2255.

Carbone, R., J. Tuttle, D. Ahijevych, and S. Trier (2002), Inferences of predictability associated with warm season precipitation episodes, *Journal of the Atmospheric Sciences*, *59*(13), 2033-2056.

Cha, J.-W., K.-H. Chang, S. S. Yum, and Y.-J. Choi (2009), Comparison of the bright band characteristics measured by Micro Rain Radar (MRR) at a mountain and a coastal site in South Korea, *Advances in Atmospheric Sciences*, *26*(2), 211-221.

Chandrasekar, V., R. Meneghini, and I. Zawadzki (2003), Global and local precipitation measurements by radar, *Meteorological Monographs*, *30*(52), 215-215.

Chen, B., J. Yang, and J. Pu (2013), Statistical Characteristics of Raindrop Size Distribution in the Meiyu Season Observed in Eastern China, *Journal of the Meteorological Society of Japan*, *91*(2), 215-227.

Chen, Y., and P. Lin (2009), The Characteristic of Drop Size Distribution During SoWMEX (in Chinese), MS thesis, 68 pp., Inst. of Atmos. Phys., Natl. Cent. Univ., Chungli, Taiwan.

Ding, Y., and J. C. Chan (2005), The East Asian summer monsoon: an overview, *Meteorology and Atmospheric Physics*, *89*(1-4), 117-142.

Fabry, F., and I. Zawadzki (1995), Long-term radar observations of the melting layer of precipitation and their interpretation, *Journal of the atmospheric sciences*, *52*(7), 838-851.

Glickman, T. S. (2000), Glossary of Meteorology, edited, Amer. Meteor. Soc.

Hamada, A., Y. N. Takayabu, C. Liu, and E. J. Zipser (2015), Weak linkage between the heaviest rainfall and tallest storms, *Nature communications*, *6*.

Hence, D. A., and R. A. Houze Jr (2011), Vertical structure of hurricane eyewalls as seen by the TRMM Precipitation Radar, *Journal of the Atmospheric Sciences*, *68*(8), 1637-1652.

Hu, Z., and R. Srivastava (1995), Evolution of raindrop size distribution by coalescence, breakup, and evaporation: Theory and observations, *Journal of the atmospheric sciences*, *52*(10), 1761-1783.

Ishimaru, A. (1991), *Electromagnetic wave propagation, radiation, and scattering*, 637 pp., Prentice-Hall.

Johnson, R. H., T. M. Rickenbach, S. A. Rutledge, P. E. Ciesielski, and W. H. Schubert (1999), Trimodal characteristics of tropical convection, *Journal of climate*, *12*(8), 2397-2418.

Löffler-Mang, M., and J. Joss (2000), An optical disdrometer for measuring size and velocity of hydrometeors, *Journal of Atmospheric and Oceanic Technology*, *17*(2), 130-139.

Lee, G. W. (2006), Sources of Errors in Rainfall Measurements by Polarimetric Radar: Variability of Drop Size Distributions, Observational Noise, and Variation of Relationships between R and Polarimetric Parameters, *Journal of Atmospheric and Oceanic Technology*, *23*(8), 1005-1028.

Liu, G., J. A. Curry, and R. S. Sheu (1995), Classification of clouds over the western equatorial Pacific Ocean using combined infrared and microwave satellite data, *Journal of Geophysical Research: Atmospheres*, *100*(D7), 13811-13826.

Liu, J., Y. Zheng, Z. Li, and M. Cribb (2011), Analysis of cloud condensation nuclei properties at a polluted site in southeastern China during the AMF-China Campaign, *Journal of Geophysical Research: Atmospheres (1984–2012)*, *116*(D16).

Liu, P., C. Y. Li, Y. Wang, and Y. F. Fu (2012), Climatic characteristics of convective and stratiform precipitation over the Tropical and Subtropical areas as derived from TRMM PR, *Science China Earth Sciences*, *56*(3), 375-385.

Marshall, J. S., and W. M. K. Palmer (1948), The distribution of raindrops with size, *Journal of meteorology*, *5*(4), 165-166.

Masunaga, H., and C. D. Kummerow (2006), Observations of tropical precipitating clouds ranging from shallow to deep convective systems, *Geophysical research letters*, *33*(16).

May, P., V. Bringi, and M. Thurai (2011), Do we observe aerosol impacts on DSDs in strongly forced tropical thunderstorms?, *Journal of the Atmospheric Sciences*, *68*(9), 1902-1910.

Milbrandt, J., and M. Yau (2005), A multimoment bulk microphysics parameterization. Part II: A proposed three-moment closure and scheme description, *Journal of the atmospheric sciences*, *62*(9), 3065-3081.

Peters, G., B. Fischer, and T. Andersson (2002), Rain observations with a vertically looking Micro Rain Radar (MRR), *Boreal environment research*, *7*(4), 353-362.

Rosenfeld, D., and C. W. Ulbrich (2003), Cloud microphysical properties, processes, and rainfall estimation opportunities, *Radar and Atmospheric Science: A Collection of Essays in Honor of David Atlas, Meteor. Monogr*, *52*, 237-258.

Rosenfeld, D., D. B. Wolff, and D. Atlas (1993), General probability-matched relations between radar reflectivity and rain rate, *Journal of applied meteorology*, *32*(1), 50-72.

Rosenfeld, D., U. Lohmann, G. B. Raga, C. D. O'Dowd, M. Kulmala, S. Fuzzi, A. Reissell, and M. O. Andreae (2008), Flood or drought: how do aerosols affect precipitation?, *science*, *321*(5894), 1309-1313.

Ryzhkov, A. V., S. E. Giangrande, and T. J. Schuur (2005), Rainfall estimation with a polarimetric prototype of WSR-88D, *Journal of Applied Meteorology*, *44*(4), 502-515.

Schönhuber, M., G. Lammer, and W. Randeu (2007), One decade of imaging precipitation measurement by 2D-video-distrometer, *Advances in Geosciences*, *10*(10), 85-90.

Short, D. A., and K. Nakamura (2000), TRMM radar observations of shallow precipitation over the tropical oceans, *Journal of Climate*, *13*(23), 4107-4124.

Streets, D. G., C. Yu, Y. Wu, M. Chin, Z. Zhao, T. Hayasaka, and G. Shi (2008), Aerosol trends over China, 1980–2000, *Atmospheric Research*, *88*(2), 174-182.

Sun, J. (2005), Initialization and numerical forecasting of a supercell storm observed during STEPS, *Monthly weather review*, *133*(4), 793-813.

Tang, Q., H. Xiao, C. Guo, and L. Feng (2014), Characteristics of the raindrop size distributions and their retrieved polarimetric radar parameters in northern and southern China, *Atmospheric Research*, *135*, 59-75.

Tao, S.-Y., and L.-X. Chen (1987), A review of recent research on the East Asian summer monsoon in China, *Monsoon Meteorology*.

Tao, W. K., J. P. Chen, Z. Li, C. Wang, and C. Zhang (2012), Impact of aerosols on convective clouds and precipitation, *Reviews of Geophysics*, *50*(2).

Testud, J., S. Oury, R. A. Black, P. Amayenc, and X. Dou (2001), The Concept of "Normalized" Distribution to Describe Raindrop Spectra: A Tool for Cloud Physics and Cloud Remote Sensing, *Journal of Applied Meteorology*, *40*(6), 1118-1140.

Thompson, E. J., S. A. Rutledge, B. Dolan, and M. Thurai (2015), Drop size distributions and radar observations of convective and stratiform rain over the equatorial Indian and West Pacific Oceans, *Journal of the Atmospheric Sciences*(2015).

Tokay, A., and D. A. Short (1996), Evidence from Tropical Raindrop Spectra of the Origin of Rain from Stratiform versus Convective Clouds, *Journal of Applied Meteorology*, *35*(3), 355-371.

Tokay, A., P. G. Bashor, E. Habib, and T. Kasparis (2008), Raindrop size distribution measurements in tropical cyclones, *Monthly Weather Review*, *136*(5), 1669-1685.

Tokay, A., W. A. Petersen, P. Gatlin, and M. Wingo (2013), Comparison of raindrop size distribution measurements by collocated disdrometers, *Journal of Atmospheric and Oceanic Technology*, *30*(8), 1672-1690.

Tsai, C.-L., and C.-K. Yu (2012), Intercomparison Analysis for Micro Rain Radar Observations (in Chinese), *atmospheric Science*, *40*(2), 109-134.

Ulbrich, C. W. (1983), Natural Variations in the Analytical Form of the Raindrop Size Distribution, *J Clim Appl Meteorol*, *22*(10), 1764-1775.

Wen, L., S. Liu, K. Zhao, Y. Li, and L. Li (2015), Precision Evaluation of Micro Rain Radar Observation in Two Precipitation Events (in Chinese), *Meteorological Monthly*, *41*(5), 577-587.

Xu, W., E. J. Zipser, and C. Liu (2009), Rainfall characteristics and convective properties of mei-yu precipitation systems over South China, Taiwan, and the South China Sea. Part I: TRMM observations, *Monthly Weather Review*, *137*(12), 4261-4275.

You, C. H., M. Y. Kang, D. I. Lee, and H. Uyeda (2014), Rainfall estimation by S-band polarimetric radar in Korea. Part I: preprocessing and preliminary results, *Meteorological Applications*.

Yu, R., and J. Li (2012), Hourly rainfall changes in response to surface air temperature over eastern contiguous China, *Journal of Climate*, *25*(19), 6851-6861.

Yuter, S. E., and R. A. Houze Jr (1995), Three-dimensional kinematic and microphysical evolution of Florida cumulonimbus. Part II: Frequency distributions of vertical velocity, reflectivity, and differential reflectivity, *Monthly weather review*, *123*(7), 1941-1963.

Zhang, G., J. Vivekanandan, and E. Brandes (2001), A method for estimating rain rate and drop size distribution from polarimetric radar measurements, *Geoscience and Remote Sensing, IEEE Transactions on*, *39*(4), 830-841.

Zhang, G., J. Sun, and E. A. Brandes (2006), Improving parameterization of rain microphysics with disdrometer and radar observations, *Journal of the atmospheric sciences*, *63*(4), 1273-1290.

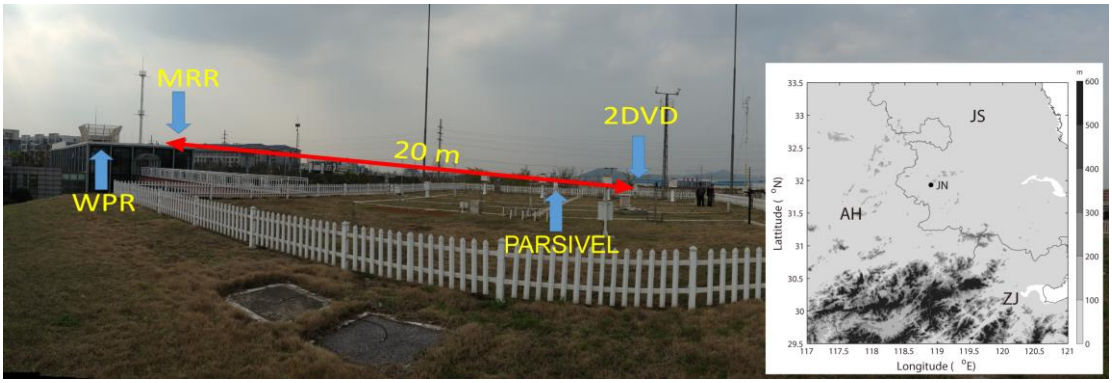

Fig. 1. Field view of the Jiangning site (JN), displaying the relative positions of the Micro-rain radar (MRR), the Wind profiler radar (WPR), the 2D-video disdrometer (2DVD) and the PARSIVEL disdrometer. The inset figure presents the local topography around the JN site.

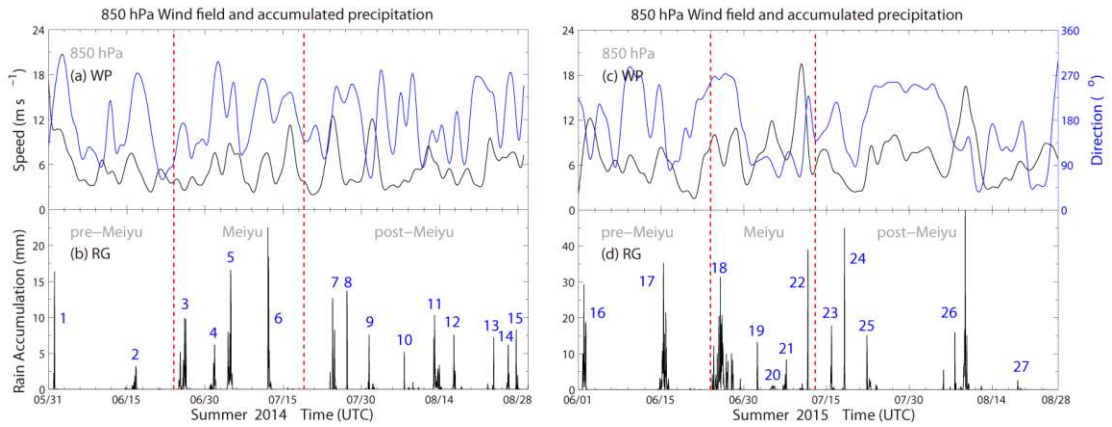

Fig. 2. The observed wind speed and direction by WPR and hourly rainfall by RG from summer 2014 and 2015. The red vertical dashed lines separate the time period into segments of pre-Meiyu, Meiyu and post-Meiyu. (a) Wind speed (black line) and wind direction (blue line); (b) time series of 27 precipitation episodes.

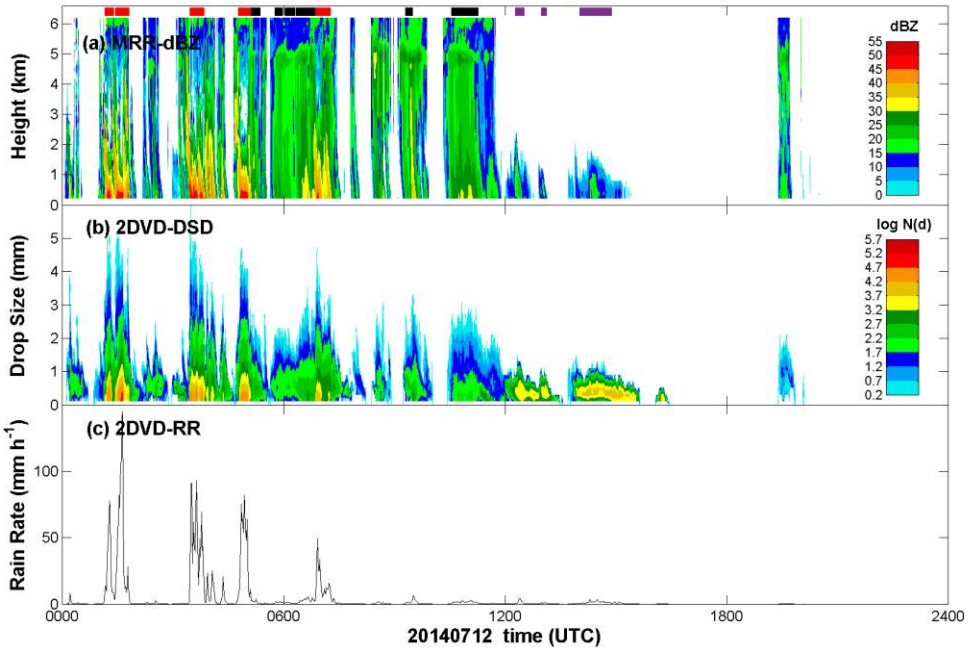

Fig. 3. The vertical profile of reflectivity from the MRR and the time series of the DSDs calculated from the 2DVD from 0000 to 2400 UTC 12 Jul 2014. (a) The color shading represents the vertical profile of reflectivity observed by the MRR. The y-axis represents the altitude. The classified convective, stratiform and shallow samples are illustrated by the red, black and purple bars on the top of the diagram. (b) The color shading represents the DSD in logarithmic units of mm^{-1} m^{-3}. The y-axis indicates the equivolume diameter (mm) of raindrops. (c) The black line represents rain rate calculated from the DSDs.

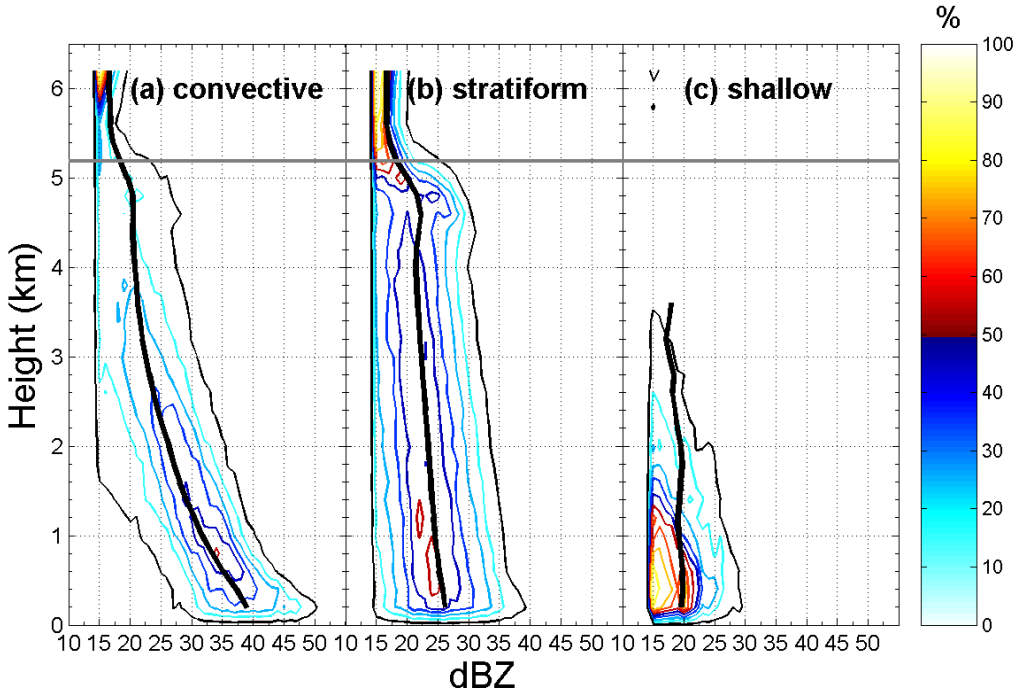

Fig. 4. Vertical profiles of reflectivity (>15 dBZ) for different rain types. Contours represent the frequency of occurrence relative to the maximum absolute frequency in the data sample represented in the CFAD, contoured every 10% with the minimum of contour-level at 5%. The ordinate of the CFAD is altitude (200-m bins) and the abscissa is reflectivity (dBZ, 1-dB bins). The black bold line that goes through each subplot represents the mean value of reflectivity. The gray line represents the mean level of the 0° C isotherm obtained from the in situ sounding data.

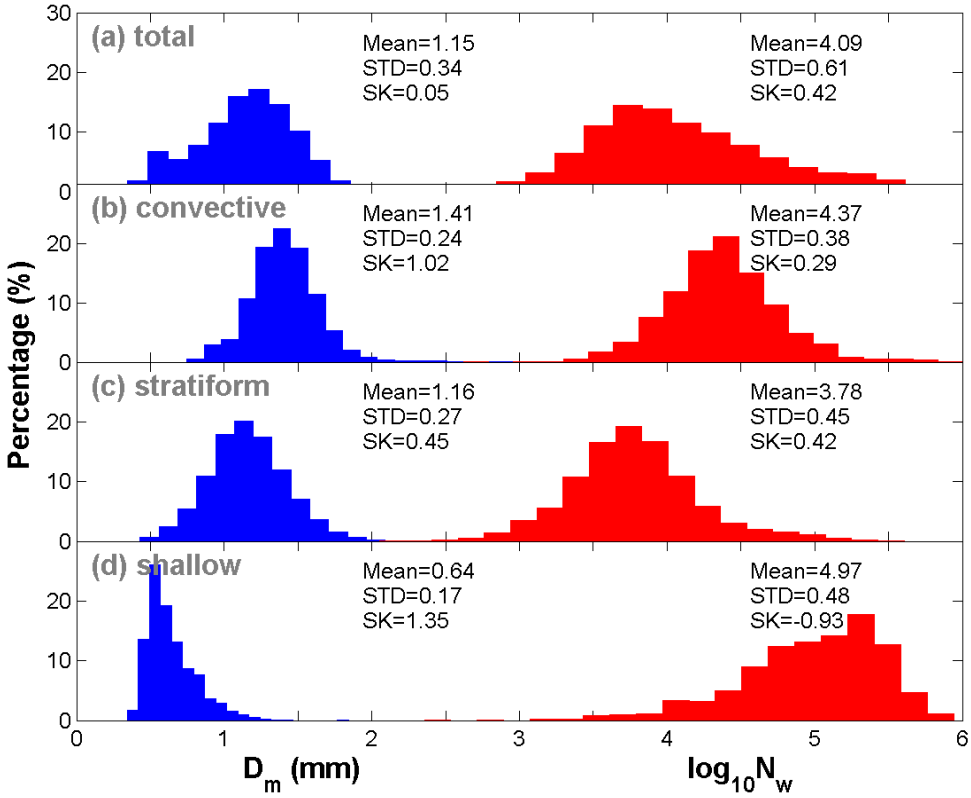

Fig. 5. Histogram of D_m and $\log_{10}N_w$ for (a) the total categorized dataset, (b) convective subset, (c) stratiform subset, and (d) shallow subset. Mean values, standard deviation (STD), and skewness (SK) are also shown in the respective panels.

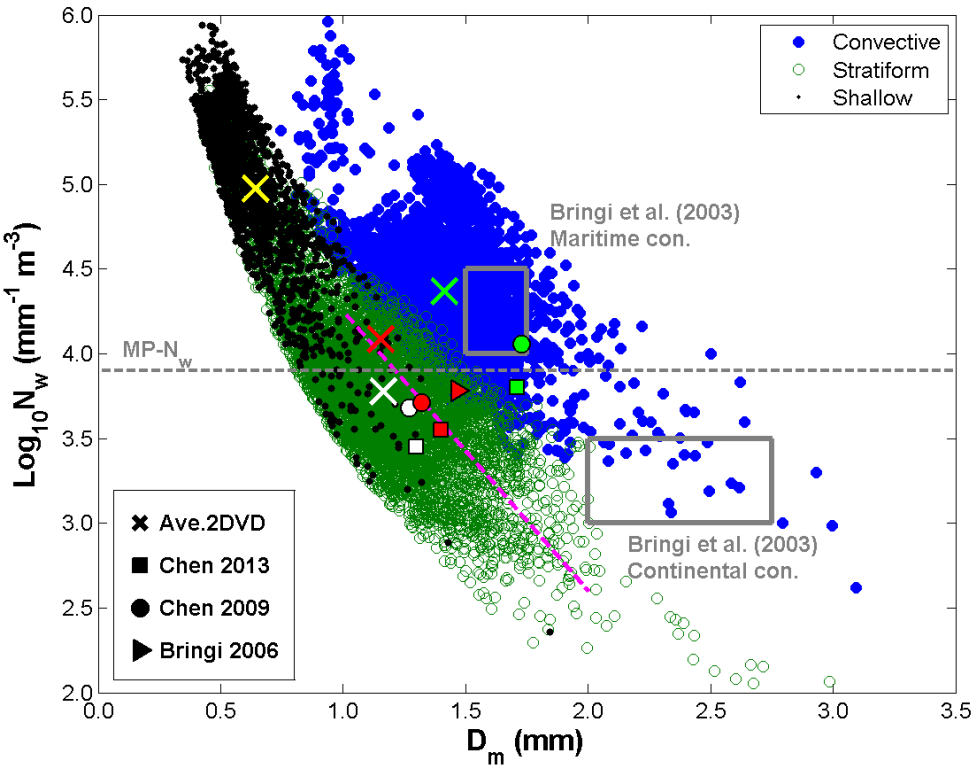

Fig. 6. Scatter plot of $\log_{10} N_w$ versus D_m for convective (blue filled circles), stratiform (green hollow circles) and shallow (black dots) rain types. The two gray rectangles correspond to the maritime and continental convective clusters reported by Bringi et al. [2003]. The square boxes, circles, and triangle represent the averaged values various types of rain, from Chen et al. [2013], Chen and Lin [2009], and Bringi et al. [2006], respectively. The red, green, white and yellow colors of these symbols are for the total categorized dataset, convective, stratiform and shallow rain, respectively. The magenta dashed line is that of Bringi et al. [2003] for stratiform rain.

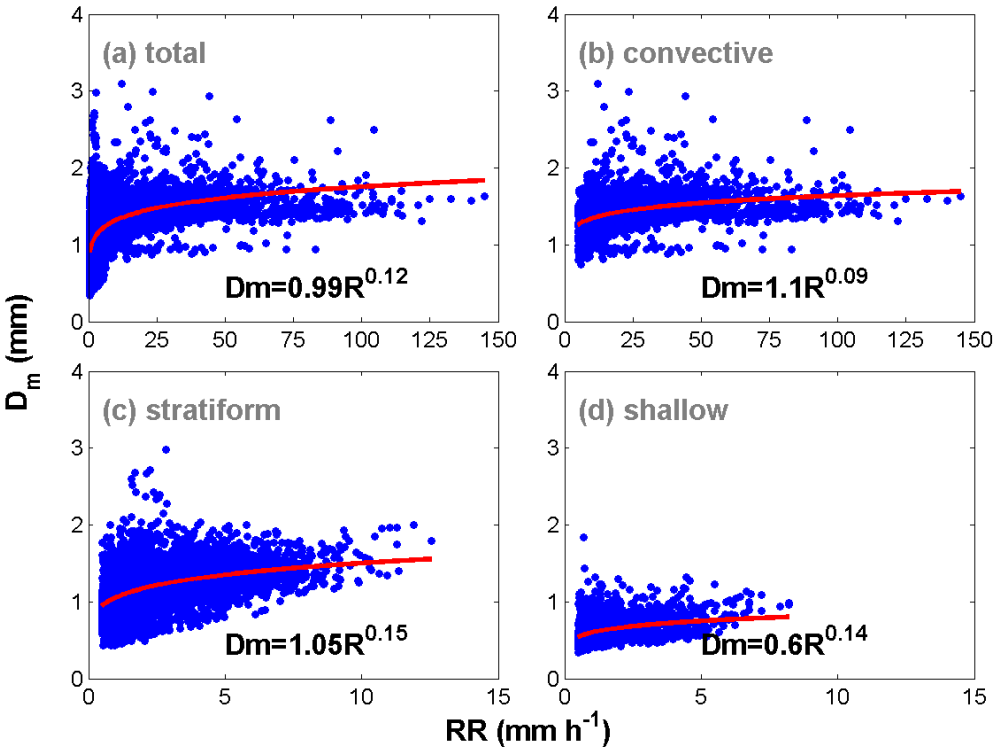

Fig. 7. Scatter plots of D_m and rain rate (RR) for (a) the total categorized dataset, (b) convective subset, (c) stratiform subset, and (d) shallow subset. The fitted power-law relationships using a least-squares method are provided in each panel.

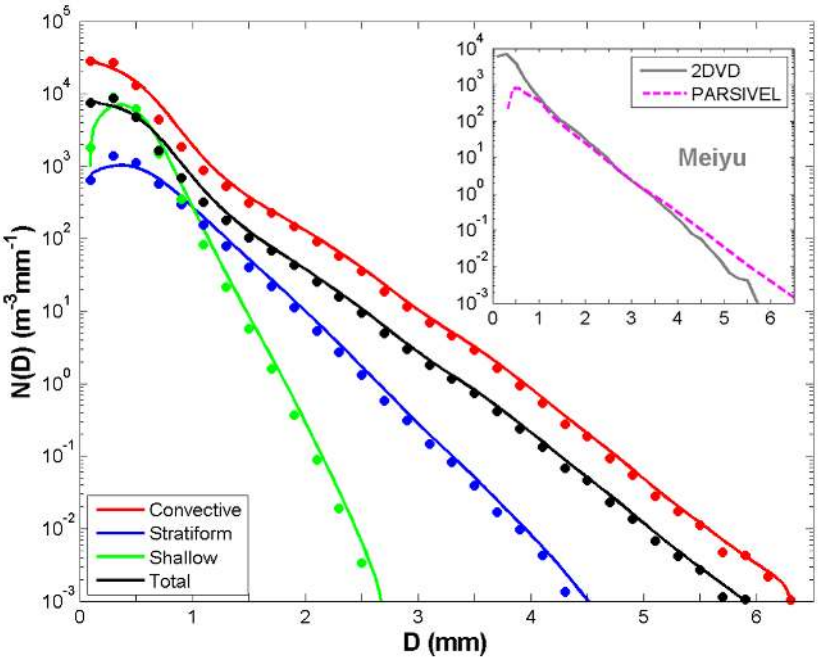

Fig. 8. Composite raindrop spectrum curves (fitted to the observations) for the convective, the stratiform and the shallow rain types, as well as for the total categorized dataset. The composite spectra of Meiyu period obtained from our 2DVD and PARSIVEL disdrometers are also provided at the upper right corner for reference.

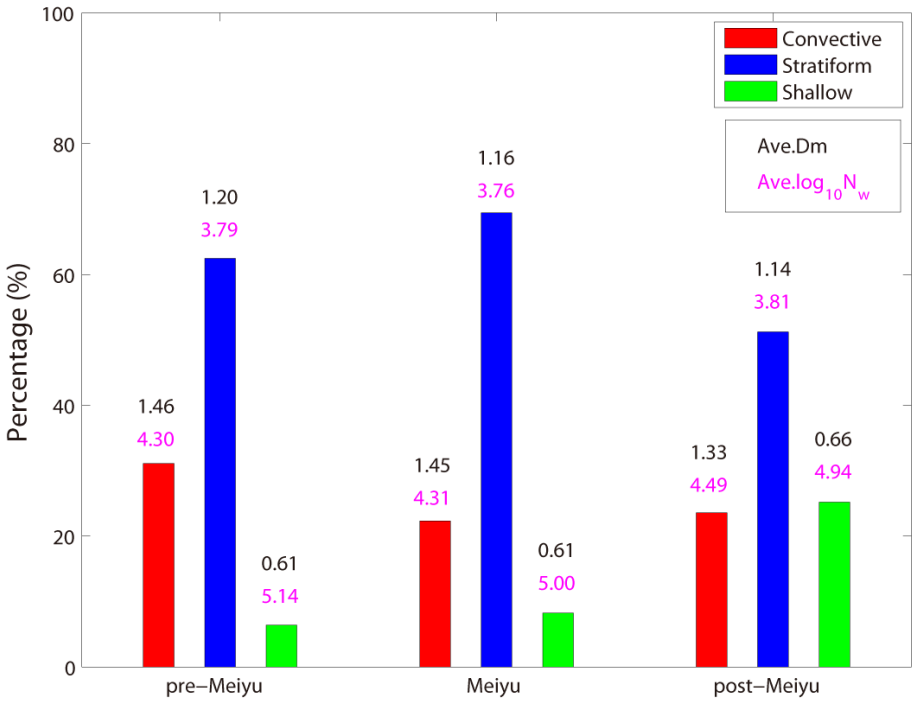

Fig. 9. The percentage occurrence of different rain types during different precipitation periods. Black and magenta numbers represent average values of D_m and $\mathrm{Log}_{10}\, N_w$.

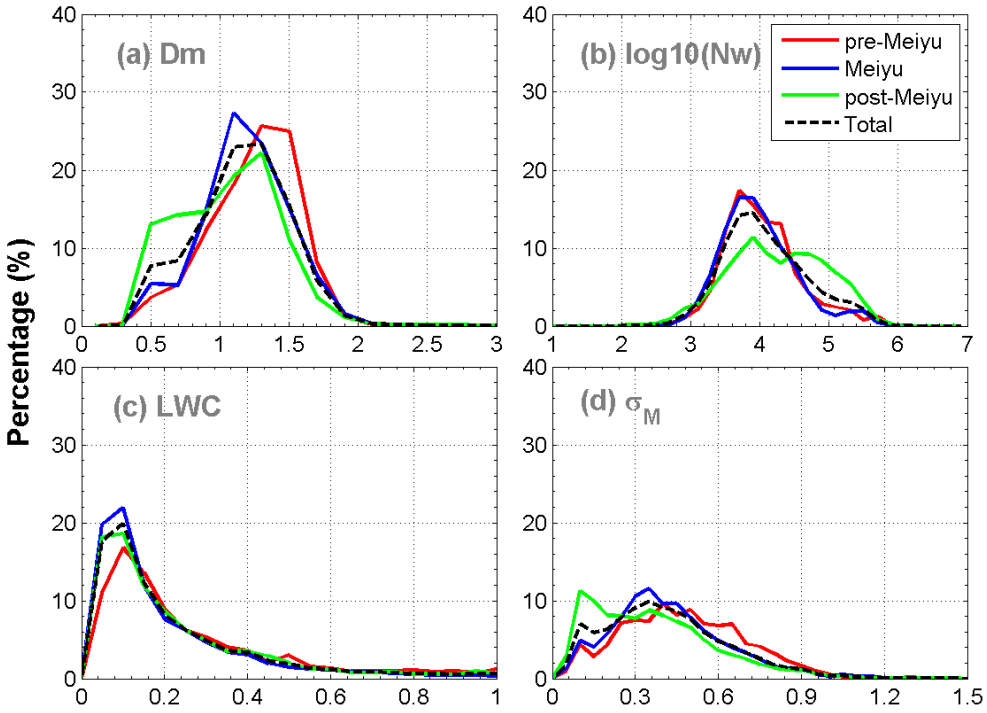

Fig. 10. The occurrence frequencies of various parameters computed from the DSDs. (a) D_m, (b) $\log_{10} Nw$ (c) LWC and (d) σ_m.

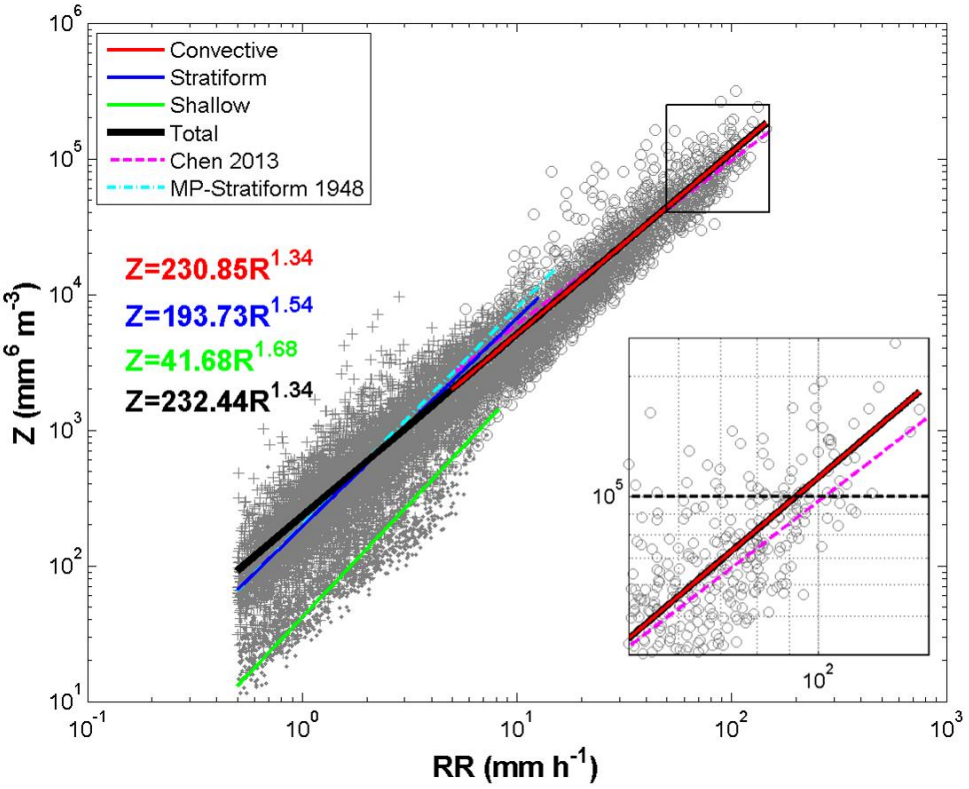

Fig. 11. Scatter plots of *Z-R* values for convective (gray circles), stratiform (gray plus signs) and shallow rain (gray dots). The fitted power-law relationships of convective, stratiform and shallow rain types in the form of $Z=AR^b$ are shown in red, blue and green solid lines. The coefficient and exponent values of the fitted power-law equations are provided. The black solid line represents the *Z-R* relationship for the total categorized dataset. The relation for continental-stratiform rain [*Marshall and Palmer*, 1948] and Meiyu-convective rain [*Chen et al.*, 2013] are provided in dashed cyan and magenta lines, respectively. The inset plot represents the amplified black rectangle region at the upper right corner.

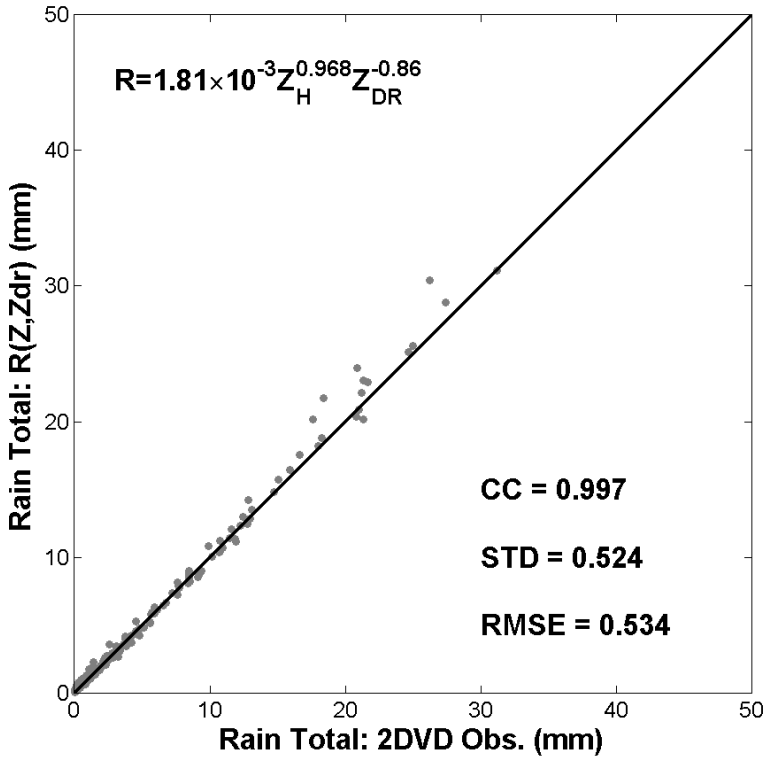

Fig. 12. Scatter plots of 2DVD observed hourly rainfall against rainfall amounts obtained from the rainfall estimation relationship $R(Z_H, Z_{DR})$. Data came from the measured DSDs at Jiangning site assuming a Brandes drop shape. Some important statistical parameters are summarized. CC, STD, RMSE are the correlation coefficient, standard deviation and root mean square error of rainfall estimate, respectively.

Table 1. Precipitation episodes used for the present study and accumulated precipitation from rain gauge.

Episode no.	Date	Accumulated precipitation (mm)	Samples (min)	Mean rain rate (mm h^{-1})	Max rain rate (mm h^{-1})
1	31 May-1 Jun 2014	26.5	189	8.4	88.7
2	16 Jun 2014	17.7	259	4.1	16.6
3	24-27 Jun 2014	67.2	858	4.7	43.4
4	1-2 Jul 2014	30.0	399	4.5	37.4
5	4-5 Jul 2014	83.2	1005	5.0	114.4
6	12 Jul 2014	72.0	321	13.5	145.1
7	24-25 Jul 2014	40.2	337	7.2	26.2
8	27 Jul 2014	25.5	113	13.5	72.8
9	31 Jul-1 Aug 2014	15.1	101	9.0	70.5
10	8-9 Aug 2014	8.2	89	5.5	10.6
11	12-14 Aug 2014	56.5	642	5.3	47.6
12	16-18 Aug 2014	22.3	238	5.6	36.9
13	24 Aug 2014	8.7	20	26.1	52.4
14	26-27 Aug 2014	16.4	220	4.5	18.2
15	28-30 Aug 2014	16.7	138	7.3	104.2
16	1-2 Jun 2015	143.8	600	14.4	122.1
17	15-17 Jun 2015	171.0	894	11.5	114.7
18	25-30 Jun 2015	364.4	1706	12.8	110.8
19	3 Jul 2015	18.3	41	26.8	81.8
20	5-6 Jul 2015	10.6	472	1.3	3.8
21	7-8 Jul 2015	21.9	335	3.9	63.9
22	11-12 Jul 2015	51.0	147	20.8	117.9
23	16-19 Jul 2015	122.8	473	15.6	106.1
24	23 Jul 2015	39.1	423	5.5	88.1
25	24-25 Jul 2015	3.4	35	5.8	16.4
26	8-10 Aug 2015	196.4	919	12.8	114.2
27	19-20 Aug 2015	5.2	27	12.2	35.1

Table 2. Frequency of precipitation of the classified rain types. The percentage refers to the contribution of each rain type to the total categorized rainfall amount.

Rain type	Samples (min)	R (mm h^{-1})	Accumulated Rainfall (mm)	Percentage (%)
Convective	2701	24.44	1100.2	77.5
Stratiform	6882	2.35	269.4	19.0
Shallow	1530	1.95	49.7	3.5
Total	11113	7.66	1419.3	100

Table 3. Integral rain parameters derived from the composite raindrop spectra. Parameters N_T, N_w, LWC, R, D_m and D_0 are the total raindrop concentration, generalized raindrop concentration, liquid water content, rain rate, mass-weighted mean diameter, and maximum raindrop diameter, respectively.

Rain type	Samples (min)	N_T (m^{-3})	$\log_{10} N_w$ (m^{-3} mm^{-1})	LWC (g m^{-3})	R (mm h^{-1})	D_m (mm)	D_{max} (mm)
Convective	2701	8079	4.37	1.50	24.4	1.41	6.3
Stratiform	6882	627	3.78	0.15	2.3	1.16	4.5
Shallow	1530	2763	4.97	0.21	1.9	0.64	2.9
Total	11113	1432	4.09	0.49	7.7	1.15	6.3

Table. 4. Integral rain parameters derived from the composite raindrop spectra for pre-Meiyu, Meiyu and post-Meiyu periods. Parameters N_T, N_w, LWC, R, D_m and D_0 are the total raindrop concentration, generalized raindrop concentration, liquid water content, rain rate, mass-weighted mean diameter, and maximum raindrop diameter, respectively.

Period	Samples (min)	N_T (m^{-3})	$\log_{10} N_w$ (m^{-3} mm^{-1})	LWC (g m^{-3})	R (mm h^{-1})	D_m (mm)	D_{max} (mm)
pre-Meiyu	1953	1700	4.03	0.57	9.2	1.24	6.3
Meiyu	5323	1184	3.99	0.44	7.2	1.18	5.7
post-Meiyu	3838	1708	4.25	0.50	7.5	1.07	5.9
Total	11113	1432	4.09	0.49	7.7	1.15	6.3